Imaging Local Electrochemical Current via Surface Plasmon Resonance

Xiaonan Shan, *et al.*

Science **327**, 1363 (2010);
DOI: 10.1126/science.1186476

17. H. J. Gao, *J. Mech. Phys. Solids* **44**, 1453 (1996).
18. E. Bouchbinder, T. S. Lo, *Phys. Rev. E Stat. Nonlin. Soft Matter Phys.* **78**, 026119 (2008).
19. E. Bouchbinder, J. Mathiesen, I. Procaccia, *Phys. Rev. Lett.* **92**, 245505 (2004).
20. K. Ravi-Chandar, B. Yang, *J. Mech. Phys. Solids* **45**, 535 (1997).
21. T. Pardoen, J. W. Hutchinson, *J. Mech. Phys. Solids* **48**, 2467 (2000).
22. I. S. Aranson, V. A. Kalatsky, V. M. Vinokur, *Phys. Rev. Lett.* **85**, 118 (2000).
23. A. Karma, D. A. Kessler, H. Levine, *Phys. Rev. Lett.* **87**, 045501 (2001).
24. See supporting material on *Science* Online.
25. R. S. Rivlin, *Philos. Trans. R. Soc. Lond. Ser. A* **240**, 459 (1948).
26. L. R. G. Treloar, *The Physics of Rubber Elasticity* (Oxford Univ. Press, New York, 1975).
27. A. Livne, G. Cohen, J. Fineberg, *Phys. Rev. Lett.* **94**, 224301 (2005).
28. A. Livne, E. Bouchbinder, J. Fineberg, *Phys. Rev. Lett.* **101**, 264301 (2008).
29. J. K. Knowles, E. Sternberg, *J. Elast.* **13**, 257 (1983).
30. E. Bouchbinder, A. Livne, J. Fineberg, *J. Mech. Phys. Solids* **57**, 1568 (2009).
31. J. K. Knowles, E. Sternberg, *J. Elast.* **3**, 67 (1973).
32. J. K. Knowles, A. J. Rosakis, *J. Appl. Mech.* **53**, 545 (1986).
33. A. M. Tarantino, *J. Elast.* **57**, 85 (1999).
34. M. Marder, *J. Mech. Phys. Solids* **54**, 491 (2006).
35. V. R. Krishnan, C. Y. Hui, R. Long, *Langmuir* **24**, 14245 (2008).
36. E. Bouchbinder, *Phys. Rev. Lett.* **103**, 164301 (2009).
37. This research was supported by grant 57/07 of the Israel Science Foundation. J.F. acknowledges the support of the Max Born Chair for Natural Philosophy.

Supporting Online Material

www.sciencemag.org/cgi/content/full/327/5971/1359/DC1
Materials and Methods
References

12 August 2009; accepted 22 January 2010
10.1126/science.1180476

Imaging Local Electrochemical Current via Surface Plasmon Resonance

Xiaonan Shan,[1,2] Urmez Patel,[1] Shaopeng Wang,[1] Rodrigo Iglesias,[1] Nongjian Tao[1,2]*

We demonstrated an electrochemical microscopy technique based on the detection of variations in local electrochemical current from optical signals arising from surface plasmon resonance. It enables local electrochemical measurements (such as voltammetry and amperometry) with high spatial resolution and sensitivity, because the signal varies with current density rather than current. The imaging technique is noninvasive, scanning-free, and fast, and it constitutes a powerful tool for studying heterogeneous surface reactions and for analyzing trace chemicals.

Electrochemical detection is a powerful analytical method that has been used for a wide range of applications, including trace chemical analysis, glucose and neurotransmitter monitoring, DNA and protein detections, and electrocatalysis studies. Measurement of the total electrochemical current or other related electrical quantities of an electrode cannot directly provide local reaction information from the electrode surface, which is required for analyses of heterogeneous reactions, local activities of cells, and protein and DNA microarrays. Scanning electrochemical microscopy (SECM) (*1*), which probes local electrochemical current by scanning a microelectrode across the surface, can overcome this limitation and has found numerous applications (*2*). However, the sequential scanning of the microelectrode limits its speed, and the scanning probe may perturb the local electrochemical processes under study. The current measured by the microelectrode in SECM scales with the size of the microelectrode, making it increasingly difficult to improve the spatial resolution by shrinking the microelectrode.

Here, we report a method for imaging local electrochemical current without the use of a scanning probe or a microelectrode. Instead of measuring the current with an electrode, it determines the electrochemical current density from an optical signal of the electrode surface generated from a surface plasmon resonance (SPR) (*3*, *4*). Important benefits of this approach include fast and noninvasive electrochemical current imaging of the surface. In addition, the measured local current signal is proportional to the optical signal, which does not scale with the area of a region of interest. We imaged local electrochemical currents generated by heterogeneous surface reactions, and we could perform the traditional electrochemical detection methods—such as amperometry, cyclic voltammetry, and square-wave voltammetry—locally, interrogating areas as small as 0.2 μm by 3 μm with a current sensitivity of 0.3 pA. We also demonstrate sensitive and selective trace analysis with the technique.

An electrochemical reaction taking place on an electrode always involves electron transfer between the electrode and the reactant, which is measured as an electrochemical current or related electrical signal in the conventional electrochemical methods. The electron transfer process is always accompanied by a conversion of chemical species between oxidized and reduced states, so the electrochemical current can be determined by monitoring the conversion of the chemical species on the surface, which is the principle of the present imaging technique. Relative to other optical detection methods such as phase-measurement microscopy (*5*) that have been used to study local molecular binding events and electrochemical reactions on surfaces (*6*, *7*), SPR is extremely sensitive to the species generated (or consumed) on the electrode surface (Fig. 1A). We show that the concentration of the species is directly related to the electrochemical current via Fick's law of diffusion (*8*); more important, the electrochemical current density $i(t)$ can be easily calculated from the local SPR signal according to

$$i(t) = bnFL^{-1}[s^{1/2}\Delta\tilde{\theta}_{SPR}(s)] \quad (1)$$

(*9*), where $b = [B(\alpha_R D_R^{-1/2} - \alpha_O D_O^{-1/2})]$, n is the number of electrons involved in the redox reaction, F is the Faraday constant, L^{-1} is the inverse Laplace transform, and $\Delta\tilde{\theta}_{SPR}(s)$ is the Laplace transform of the SPR signal. In the expression for b, α_O and α_R are the changes in the local refractive indices per unit concentration for the oxidized and reduced molecules, D_O and D_R are the diffusion coefficients of the oxidized and reduced molecules, and B measures the sensitivity of the SPR signal to a change in the bulk index of refraction, which can be calibrated independently. According to Eq. 1, the measured signal, $i(t)$, does not scale with the image area, which is in contrast to the conventional electrochemical detection methods. Note that double layer charging current also contributes to the SPR signal (*10*), which is, however, small (*11*) relative to faradaic current.

We show below that (i) the electrochemical current determined using Eq. 1 is indeed equivalent to that obtained from the conventional electrochemical methods; (ii) the new electrochemical imaging technique provides local electrochemical current (e.g., cyclic voltammograms) associated with heterogeneous surface reactions; (iii) the advantages of this imaging technique allow for sensitive and selective trace analysis; and (iv) the technique offers high current sensitivity, a fast imaging rate, and good spatial resolution.

Two optical configurations were used in the experiments. In the first configuration, the working electrode was an Au-coated glass slide attached onto a prism via index-matching fluid. An electrochemical cell made from Teflon was mounted on top of the Au electrode. A Pt wire counterelectrode and an $Ag|AgCl|KCl_{(sat.)}$ reference electrode, together with a potentiostat, were used to control the potential of the working electrode. A light-emitting diode (LED) with a peak wavelength of 670 nm was used to excite the surface plasmons in the Au electrode, and a charge-coupled device (CCD) camera was used to record the image. Calculating the current at each pixel from the image by means of Eq. 1 creates an elec-

[1]Center for Bioelectronics and Biosensors, Biodesign Institute, Arizona State University, Tempe, AZ 85287, USA. [2]Department of Electrical Engineering, Arizona State University, Tempe, AZ 85287, USA.

*To whom correspondence should be addressed. E-mail: njtao@asu.edu

trochemical current image, and plots of the current image versus time or potential provide local amperometric and voltammetric measurements of the electrode. The second configuration (Fig. 1A) used an oil immersion objective with a high numerical aperture of 1.65 (*12*) to replace the prism and a HeNe laser to replace the LED. This second configuration provided higher spatial resolution than the first configuration.

To demonstrate the imaging principle, we studied the redox reaction of $Ru(NH_3)_6^{3+}$ complex with conventional cyclic voltammetry and electrochemical imaging simultaneously. The conventional method measures the total electrochemical current of the entire electrode surface, and the voltammogram shows the characteristic redox peaks corresponding to the reduction and oxidation of the ruthenium complex (Fig. 1B, red line). The electrochemical imaging technique probes the local electrochemical current, so the current averaged over the entire surface versus the potential (Fig. 1B, open circles) is compared with the conventional voltammetry. The cyclic voltammograms obtained by the two methods are in good agreement with each other (overall deviation = 5.75%). Note that the parameter *b* in Eq. 1 was calibrated independently from a separate experiment (*9*), so the agreement between the voltammograms obtained with the conventional and present imaging methods is quantitative and involves no adjustment of parameters.

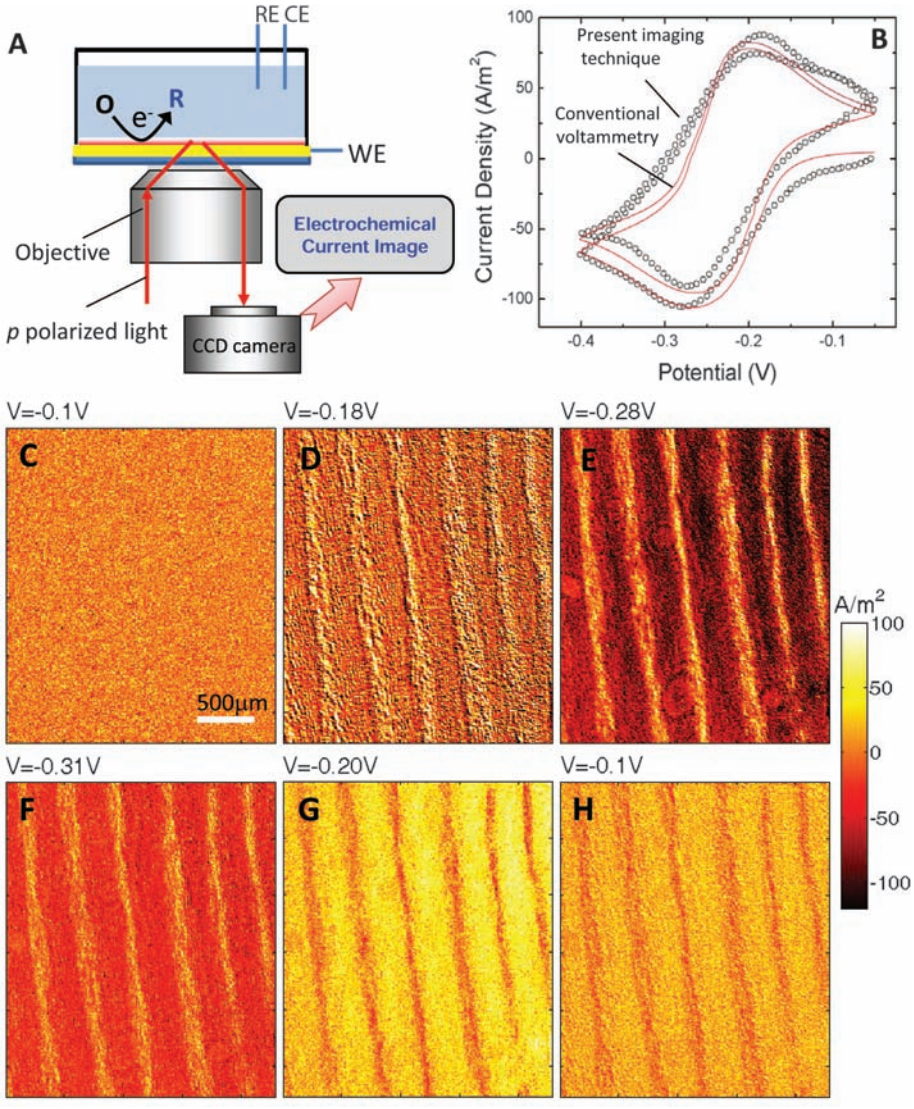

Fig. 1. (**A**) Schematic illustration of an electrochemical current imaging technique, where RE, CE, and WE are reference, counter, and working electrodes, respectively. (**B**) Cyclic voltammograms measured by the conventional electrochemical method (red line) and by the electrochemical current imaging technique (open circles) of a bare gold electrode. Note that for a close comparison between the two approaches, the cyclic voltammogram from the imaging technique is averaged over the entire electrode surface. The electrolyte is 0.25 M phosphate buffer containing 10 mM $Ru(NH_3)_6^{3+}$, and the potential sweep rate is 0.1 V/s. (**C** to **H**) Electrochemical current images of a fingerprint at different potentials recorded during continuous cycling of the electrode potential between –0.10 V and –0.35 V at a rate of 0.1 V/s (see movie S1). The electrolyte is 0.25 M phosphate buffer containing 10 mM $Ru(NH_3)_6^{3+}$.

One of the most important applications of the technique is imaging of the local electrochemical current associated with heterogeneous reactions. To demonstrate this capability, we created a fingerprint (*13*) on an Au electrode by touching it, which transferred the secretions from the skin ridges of the finger onto the electrode surface. We imaged the local electrochemical current of the surface by cycling the electrode potential in an electrolyte [0.25 M phosphate buffer containing 10 mM $Ru(NH_3)_6^{3+}$]. Figure 1, C to F, shows several snapshots of the electrochemical current video (movie S1) at different potentials. At –0.10 V, far away from the redox potential, almost no electrochemical reaction takes place and the image does not show any contrast (Fig. 1C). As the potential decreases, reduction of $Ru(NH_3)_6^{3+}$ takes place and the contrast of the fingerprint begins to show up (Fig. 1D). At –0.28 V, the contrast reaches maximum, corresponding to the maximum reduction current (Fig. 1E). As the potential cycles back toward positive values, the contrast is inverted (Fig. 1G), which reflects a sign change in the electrochemical current (from reduction to oxidation). Finally, when the potential cycles back to –0.10 V, the contrast disappears nearly completely; the small remaining contrast is the result of residual electrochemical reactions at the potential, in agreement with the cyclic voltammetry, which shows a finite current when the potential returns to the starting value (Fig. 1B). The entire process was repeated by continuously cycling the potential. Note that the imaging speed is solely determined by the CCD imager, which was ~2000 frames/s in the present setup, much faster than the SECM rate.

The contrast of the fingerprint revealed by the electrochemical current images arises from the blockade of the electrochemical reactions in the regions covered by the secretions from the finger. This interpretation is directly confirmed by the conventional SPR image acquired on the same electrode by switching off the potential (Fig. 2A). The regions covered with the secretions are shown as positive contrast in the SPR image, from which we estimated the average thickness of the fingerprint to be ~2.5 nm. This thin layer of molecules blocks the electrochemical reaction of the redox molecules. The fact that conventional SPR images can also be obtained using the same optics provides additional value to the present electrochemical current imaging technique.

The snapshots in Fig. 1, C to F, show only a small fraction of the information in the time and potential sequences of the electrochemical current image. At each point of the image, a local cyclic voltammogram can be readily obtained. Figure 2, B to E, shows a few examples of local cyclic voltammograms at different locations marked in Fig. 2A. First, the voltammogram from a bare gold region shows a large electrochemical current with well-defined redox peaks (Fig. 2B). In contrast, the voltammogram from a region covered with finger secretions shows only small background current with no obvious redox peaks (Fig. 2C).

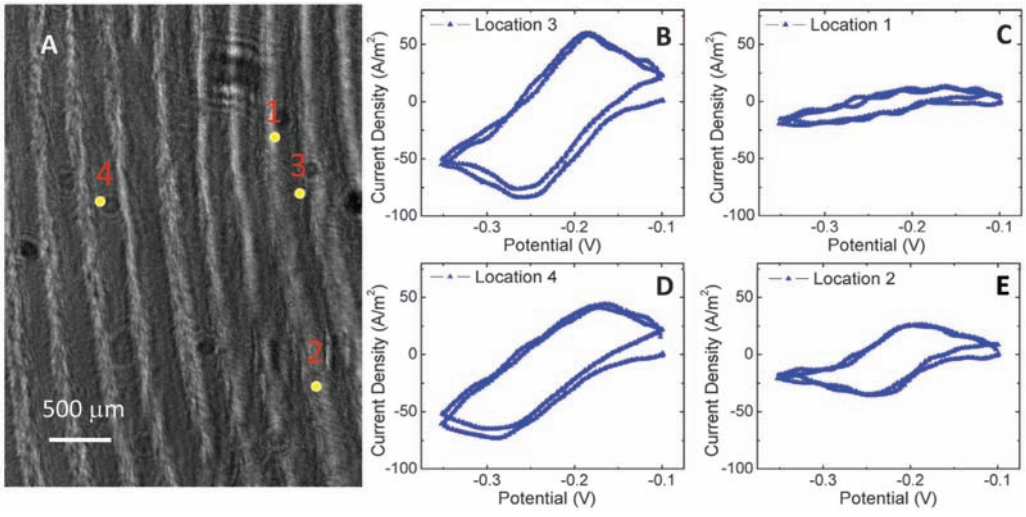

Fig. 2. (**A**) SPR image of a fingerprint. (**B** to **E**) Local cyclic voltammograms at different locations of the surface as numbered in (A). The electrolyte is 0.25 M phosphate buffer containing 10 mM $Ru(NH_3)_6^{3+}$, and the potential sweep rate is 0.1 V/s.

Second, the voltammograms obtained from different regions of a bare Au electrode also vary. For example, voltammograms from two different Au regions are shown in Fig. 2, B and D. Although both display the well-defined redox peaks, the separations of the redox peaks are quite different, which is likely a result of the variation in the coverage of the secretions transferred from the finger. Finally, the voltammograms from different regions of the fingerprint are also different (Fig. 2, C and E), reflecting changes in the coverage of the finger secretions.

The capability of imaging local electrochemical current has many applications, including trace analysis. As an example, we used the technique to detect traces of trinitrotoluene (TNT) (*14*). TNT has a very low vapor pressure and often appears in the form of particulates. A small TNT particle can be visualized with an optical microscope, but it is difficult to distinguish it from dusts or other airborne particulate matter. TNT is known to undergo electrochemical reductions at certain potentials, which has led to the detection of TNT by electrochemical methods (*15*). However, if the amount of TNT particulates is small, it is difficult to detect them using conventional electrochemical detection methods that measure the total current from the entire electrode. We prepared a sample including a fingerprint and TNT particulates on the electrode surface. Although the fingerprint is visible in the SPR image, the TNT particulates could not be resolved (Fig. 3A). We recorded the electrochemical current image of the surface while cycling the potential. Figure 3B shows five snapshots at different potentials. At 0 V, the electrochemical current image shows a uniform surface with no contrast for either the fingerprint or the TNT particulates because no electrochemical reactions take place at this potential (Fig. 3B, image 1). When we sweep the potential toward negative values, contrast of the fingerprint begins to show up (Fig. 3B, image 2) from the reduction of dissolved oxygen gas in the electrolyte, which results in different electrochemical currents in the regions with and without the fingerprint secretions. At this point, it is still

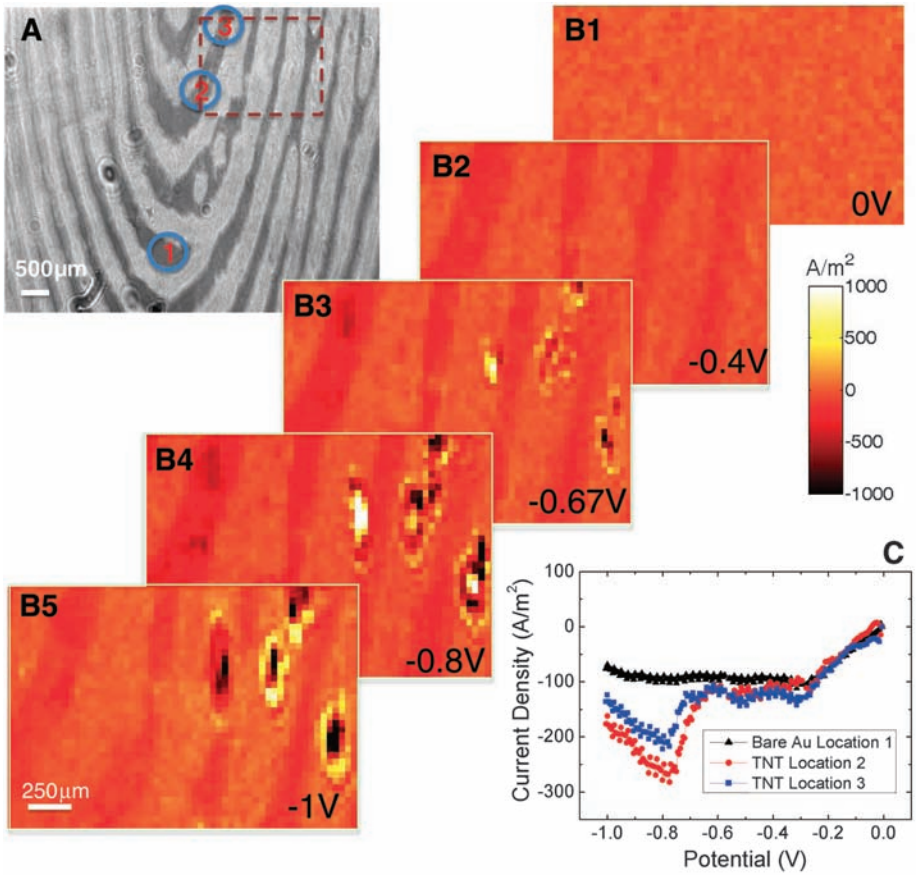

Fig. 3. Detection of TNT traces on a fingerprint using the electrochemical current imaging technique. (**A**) SPR image of a fingerprint. (**B**) Five snapshots recorded while sweeping the potential negatively from 0 to −1.0 V at a rate of 0.05 V/s. The appearance of the "spots" is due to the reduction of TNT particulates. (**C**) Local voltammograms of the regions with (blue and red dots) and without (black dots) TNT particulates. The electrolyte is 0.5 M KCl.

difficult to resolve features attributable to the TNT particulates. When we lower the potential further toward the reduction potential of TNT, "spots" in the electrochemical current image associated with the reduction of the TNT particulates begin to appear (Fig. 3B, images 3 to 5), which allow us to detect and identify the individual TNT particulates.

By selecting regions where "spots" appear, we obtained local voltammograms showing peaks from the reduction of TNT (Fig. 3C). For comparison, a local voltammogram from a region without TNT is also shown (black dots, Fig. 3C). We note that the TNT peak shapes and positions are not exactly the same as those in the cyclic

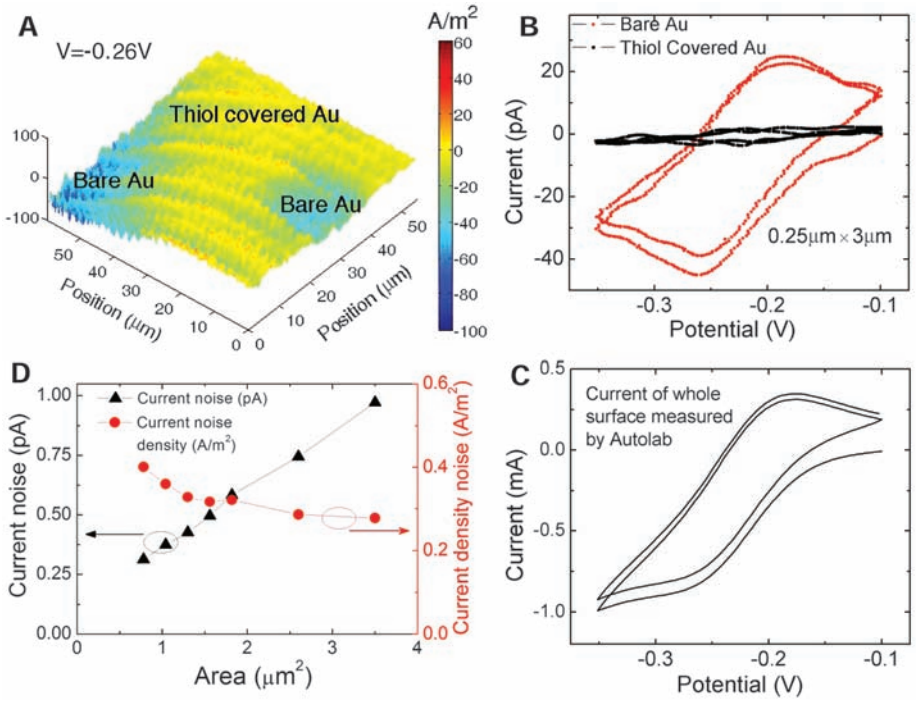

Fig. 4. Spatial resolution and current detection limit. (**A**) Electrochemical current image of 1-hexadecanethiol self-assembled on an Au electrode in 0.25 M phosphate buffer containing 10 mM $Ru(NH_3)_6^{3+}$, where the blue regions (negative current) are due to the reduction of $Ru(NH_3)_6^{3+}$. (**B**) Cyclic voltammograms of regions covered with densely packed (black lines) and exposed gold (red lines) regions. (**C**) Cyclic voltammogram obtained with the conventional electrochemical method (that measured the current over the entire electrode surface). (**D**) Dependence of current noise and current density noise on the area of detection.

voltammograms of TNT dissolved in an electrolyte as measured by the conventional electrochemical method (*16*). The difference may arise from differences in the mass transport between two experiments. From the integrated area of the reduction current peak at –0.8 V shown in the local voltammograms (Fig. 3C), we estimated the mass of the corresponding TNT particulate to be as small as ~0.5 ng (for an area of 50 μm by 50 μm). Because the current detection limit is ~0.3 pA (see below), the estimated detection limit is 0.3 fg.

We also used the conventional electrochemical method to record the voltammogram of the surface and did not observe the distinctive reduction peaks of TNT (fig. S1); the TNT signal was washed out by the large background current from areas without TNT. In contrast, the present electrochemical imaging technique obtains the local voltammograms of the particulate regions, which eliminates the background current contribution from other regions to the measured signal. The capability of performing local electrochemical analysis on the regions of interest (determined by the image) also reduces potential interference in electrochemical analysis. For instance, the large electrochemical reduction peak of the dissolved oxygen—a known source of interference taking place over the entire electrode surface—does not substantially affect the local voltammogram of a small particulate region.

Conventional optical imaging techniques, including SPR, can resolve small particles, but they usually cannot reveal the chemical identities of the particles. To further demonstrate the capability of trace chemical analysis with the imaging technique, we introduced other particulate matter, such as candle wax, onto the fingerprint in the presence of TNT particulates. The conventional SPR could image but could not distinguish the two types of particles (fig. S2). However, the electrochemical current image shows the distinct contrast changes in the regions of TNT particulates associated with the electrochemical reduction.

We now examine the spatial resolution and current detection limit of the electrochemical imaging technique. The spatial resolution along the surface plasmon propagation direction is limited by the propagation length, which depends on the wavelength of light. For a wavelength of 638 nm, the propagation length is ~3.1 μm; for a wavelength of 532 nm, the propagation length decreases to 0.2 μm (*12*). In the direction perpendicular to the surface plasmon propagation, the resolution is limited by the optical diffraction limit, which is about 0.19 μm using an objective with numerical aperture of 1.65. An electrochemical current imaging of a 1-hexadecanethiol–patterned electrode created by polydimethylsiloxane (PDMS) contact printing (*17*) is shown in Fig. 4A, where the current contrast arises from the variation in the coverage of the self-assembled monolayer. The local voltammogram from a gold surface region (0.25 μm by 3 μm) covered with densely packed 1-hexadecanethiol shows little current (Fig. 4B, black line). In contrast, the voltammogram from a region without covering of 1-hexadecanethiol (0.25 μm by 3 μm) shows well-defined redox peaks that are separated with ~60 mV, as expected for a reversible redox reaction (Fig. 4B, red line). In contrast, the simultaneously recorded voltammogram with the conventional electrochemical method shows distorted redox peaks caused by averaging of different reactions over the entire electrode (Fig. 4C).

This imaging technique measures light intensity, corresponding to current density, which does not decrease with the size of an imaged area, so high spatial resolution does not compromise the current detection limit. As shown in Fig. 4D, the noise level in the current density (red circles) does not change much with the area, so the noise in the current decreases with the area (black triangles). The smallest meaningful area is determined by the spatial resolution, which is ~0.2 μm by ~3 μm. The noise from such a small region in our present setup is ~0.3 pA. This level of current noise is excellent relative to other electrochemical detection methods, typically in the picoampere to nanoampere range (*18*), and could be further optimized by improving the light source and CCD detector. The electrode used here is gold, and other metal electrodes (e.g., Ag, Cu, and Pt) can also be used. Just like the current-based electrochemical detections, an electrochemical reaction is always accompanied by a change in the chemical species, so the electrochemical current imaging technique described here is universal.

References and Notes

1. A. J. Bard *et al.*, *Science* **254**, 68 (1991).
2. S. Amemiya, A. J. Bard, F. R. F. Fan, M. V. Mirkin, P. R. Unwin, *Annu. Rev. Anal. Chem.* **1**, 95 (2008).
3. B. Rothenhäusler, W. Knoll, *Nature* **332**, 615 (1988).
4. J. M. Brockman, B. P. Nelson, R. M. Corn, *Annu. Rev. Phys. Chem.* **51**, 41 (2000).
5. Q. G. Li, H. S. White, *Anal. Chem.* **67**, 561 (1995).
6. G. Flätgen *et al.*, *Science* **269**, 668 (1995).
7. O. Andersson, C. Ulrich, F. Bjorefors, B. Liedberg, *Sens. Actuators B Chem.* **134**, 545 (2008).
8. A. J. Bard, L. R. Faulkner, *Electrochemical Methods* (Wiley, New York, 1980).
9. See supporting material on *Science* Online.
10. D. G. Hanken, C. E. Jordan, B. L. Frey, R. M. Corn, *Electroanal. Chem.* **20**, 141 (1998).
11. K. J. Foley, X. Shan, N. J. Tao, *Anal. Chem.* **80**, 5146 (2008).
12. B. Huang, F. Yu, R. N. Zare, *Anal. Chem.* **79**, 2979 (2007).
13. M. Zhang, H. H. Girault, *Analyst* **134**, 25 (2009).
14. L. A. Pinnaduwage *et al.*, *Nature* **425**, 474 (2003).
15. J. Wang, *Electroanalysis* **19**, 415 (2007).
16. H. X. Zhang, A. M. Cao, J. S. Hu, L. J. Wan, S. T. Lee, *Anal. Chem.* **78**, 1967 (2006).
17. N. L. Abbott, J. P. Folkers, G. M. Whitesides, *Science* **257**, 1380 (1992).
18. The current noise value depends on bandwidth, instruments, and other experimental details.

19. We thank H. H. White, E. Forzani, and A. Cagan for discussions and L. Zhang for help in the lab. Supported by NSF grant CHM-0554786.

Supporting Online Material

www.sciencemag.org/cgi/content/full/327/5971/1363/DC1
Materials and Methods
SOM Text
Figs. S1 and S2
Movie S1
References

28 December 2009; accepted 3 February 2010
10.1126/science.1186476